RSC Advances

RSC Publishing

PAPER

View Article Online
View Journal | View Issue

Non-stoichiometry in "$CaCu_3Ti_4O_{12}$" (CCTO) ceramics†

Rainer Schmidt,*[a] Shubhra Pandey,[bc] Patrick Fiorenza[d] and Derek C. Sinclair[b]

Cite this: *RSC Advances*, 2013, **3**, 14580

Received 19th March 2013,
Accepted 24th May 2013

DOI: 10.1039/c3ra41319e

www.rsc.org/advances

A combined powder X-ray lattice parameter and ceramic impedance spectroscopy study is presented on materials within the CaO–CuO–TiO_2 ternary phase diagram. Several compositions containing $CaCu_3Ti_4O_{12}$ (CCTO) and small amounts of secondary phases such as TiO_2, $CaTiO_3$ and CuO are analysed and two different defect mechanisms are identified as the cause of the non-stoichiometry in CCTO. The first mechanism involves a variation in the Cu content, which explains the large differences in the intrinsic bulk and extrinsic grain boundary (GB) resistance, and the formation of the ceramic internal barrier layer capacitor (IBLC) structure. The second mechanism is associated with Ca–Cu anti-site disorder causing an unusually high intrinsic bulk permittivity above that predicted from Clausius–Mossotti calculations.

I. Introduction

The ternary oxide compound $CaCu_3Ti_4O_{12}$ (CCTO) is a 1 : 3 A-site ordered perovskite ($A'A''_3B_4O_{12}$) where the oxygen octahedra are strongly tilted and the A'' site Cu cations adapt a fourfold square–planar coordination. The CCTO unit cell is a doubled simple perovskite cell and is commonly indexed as cubic $Im\bar{3}$.[1,2] The octahedral tilting can be described as $a^+a^+a^+$ in the Glazer notation.[3–5]

CCTO has attracted considerable interest due to its giant dielectric permittivity values;[6–11] in polycrystalline ceramics the highest values reported are $\approx$ 300 000.[12] It is now well established that such high permittivity values have an extrinsic origin.[13,14] In ceramics, an internal barrier layer capacitor (IBLC) structure has been proposed that is made up of semiconducting grains and insulating grain boundaries (GBs), where the extrinsic giant permittivity ε_{GB} would be called a GB effect.[15] In single crystals and epitaxial thin films, giant permittivity can be associated with an extrinsic electrode–sample interface effect,[16,17] which can also contribute to the giant permittivity in ceramics.[18] The intrinsic relative dielectric permittivity, ε_b, of bulk CCTO was reported to be around 100.[14] While this is considerably lower than the giant extrinsic values, it is still higher than would be expected in a non-ferroelectric material based on the polarizabilities of the constituent atoms[19] as predicted by the Clausius–Mossotti equation (*i.e.*, ε_b in CCTO is expected to be $\approx$ 48). The difference in electrical conductivity between the GB and bulk areas in CCTO is large: the GB charge transport activation energy E_A is about 0.5–0.8 eV, while the bulk E_A is about 10–100 meV,[15,20] additionally, the nominal resistance of the GB and bulk areas vary by a factor of up to $\approx 10^5$. Considering that the GB areas are expected to be thin layers the actual difference in resistivity may be even more dramatic. It was shown previously that this distinct ceramic IBLC structure becomes more pronounced during the ceramic sintering process and is associated with segregation of Cu towards the GB areas.[21] More recently it was shown that the interior conducting grain phase of CCTO in fact grows out of an insulating matrix during sintering, most likely by segregation of Cu out of the conducting areas.[22] Here, in this work, such Cu segregation is explicitly associated with a defect mechanism, which offers a plausible explanation for the large differences in conductivity between the bulk and GB regions. A second defect mechanism is associated with the Ca–Cu anti-site defects and the increased ε_b bulk permittivity.

In the literature the CCTO bulk semiconductivity has been associated with quite different and often contradictory defect mechanisms for this nominally insulating compound. It is generally agreed that deviations from the nominal $CaCu_3Ti_4O_{12}$ stoichiometry must exist in bulk areas to explain their semiconductivity, and that the insulating GBs would exhibit smaller or no deviations.[23–25] Several defect mechanisms suggested in the literature are contradictions because they imply that different types of bulk semiconductivity are occurring, *i.e.* n-type electron or p-type hole conduction. Semiconductivity in bulk CCTO could potentially rely on mixed valence Ti^{3+}/Ti^{4+} or Cu^{1+}/Cu^{2+} (n-type), or Cu^{2+}/Cu^{3+} (p-type) conduction. All defect mechanisms, solid solutions and possible compensation mechanisms reported in the literature[23–25] are summarised below in eqn (A–D). A further

[a]*Universidad Complutense de Madrid, Departamento Física Aplicada III, GFMC, Facultad de Ciencias Físicas, 28040 Madrid, Spain.*
E-mail: rainerxschmidt@googlemail.com
[b]*The University of Sheffield, Materials Science and Engineering, Mappin Street, Sheffield, S1 3JD, United Kingdom*
[c]*Indian Institute of Technology Kanpur, Department of Materials Science and Engineering, Kalyanpur, Kanpur - 208 016, India*
[d]*CNR-IMM, Strada VIII n.5, Zona Industriale, 95121 Catania, Italy*
† Electronic supplementary information (ESI) available. See DOI: 10.1039/c3ra41319e

mechanism appears to be plausible from the work presented here, shown in eqn (E). Brackets ( ) are used to indicate the A′′ Cu sites.

$$O_o^{2-} + 2Ti^{4+} \rightarrow V_0^{\cdot\cdot} + 2Ti^{3+}\ 1/2O_2\uparrow\ :\ Ca(Cu_3)Ti_{4-u}^{4+}Ti_u^{3+}O_{12-u/2} \quad (A)$$

$$3Cu^{2+} \rightarrow 2Cu^{1+} + Ti_{Cu}^{4+} + Cu\uparrow\ :\ Ca(Cu_{3-3v}^{2+}Cu_{2v}^{1+}Ti_v^{4+})Ti_4O_{12} \quad (B)$$

$$Cu^{+} + Ti^{4+} \rightarrow Cu^{2+} + Ti^{3+}\ :\ Ca(Cu_{3-v}^{2+}Ti_v^{4+})\ Ti_{4-2v}^{4+}Ti_{2v}^{3+}O_{12} \quad (C)$$

$$3\ Cu^{2+} \rightarrow V_{Cu}^{''} + 2Cu^{3+} + Cu\uparrow\ :\ Ca(Cu_{3-3v}^{2+}Cu_{2v}^{3+}V''_v)Ti_4O_{12} \quad (D)$$

$$O_o^{2-} + Ti^{4+} \rightarrow V_0^{\cdot\cdot} + Cu_{Ti}^{2+} + 1/2O_2\uparrow\ :\ Ca(Cu_3^{2+})Ti_{4-w}^{4+}Cu_w^{2+}O_{12-w} \quad (E)$$

Eqn (A) represents oxygen loss and the formation of oxygen vacancies, which is a common phenomenon in perovskite and related structures.[26,27] Compensation occurs by $Ti^{4+} \rightarrow Ti^{3+}$ reduction. Eqn (B) represents loss or deficiency of Cu, which is compensated for by the partial reduction of Cu^{2+} to Cu^{+} and partial occupation of the Cu sites by Ti^{4+}. Processes in (A) and (B) would most likely take place during heat treatment at elevated temperatures under inert or reducing conditions. In eqn (C) the Cu^{2+} reduction at elevated temperatures described in eqn (B) is now assumed to be fully reversible upon cooling *via* reoxidation, whereas the Cu deficiency persists. The reoxidation of $Cu^{+} \rightarrow Cu^{2+}$ in turn is compensated for by the partial reduction of $Ti^{4+} \rightarrow Ti^{3+}$ *i.e.*, an internal redox process takes place. Only the redox process is displayed in eqn (C) as the high temperature Cu reduction is identical to eqn (B). Eqn (D) represents the loss of Cu due to Cu segregation or volatilisation and the formation of Cu vacancies. Compensation occurs *via* the partial oxidation of Cu^{2+} to Cu^{3+}. Eqn (E) corresponds to excess Cu and compensation occurs by Cu^{2+} occupying Ti sites and the formation of oxygen vacancies. Alternatively, compensation in eqn (E) could also occur *via* oxidation of Cu^{2+} to Cu^{3+} and fewer oxygen vacancies would form. Models (A), (B) and (C) are supported by the propositions of n-type conduction.[24,28] Processes (B) and (C) are consistent with the detection of Cu^{+} (ref. 29) and Ti^{3+} (ref. 29 and 30), respectively, both from XPS studies, whereas model (D) is supported by findings of (i) Cu loss;[25,31] (ii) the presence of Cu^{3+} seen in XPS studies,[25] and (iii) p-type bulk semiconductivity determined from Hall effect measurements.[17] Eqn (E) has not been mentioned in the literature, but may be applicable in Cu-rich GB areas. Furthermore, Ca^{2+} and Cu^{2+} anti-site defects have been proposed to be the origin of the high dielectric permittivity in CCTO,[32] despite the considerable mismatch between the ionic radius of Ca^{2+} (XII coordination: 1.35 Å) and Cu^{2+} (IV square planar coordination: 0.62 Å). Another possible anti-site defect mechanism may be Cu–Ti disorder, where the ionic radii are more similar *i.e.*, Cu^{2+} (VI: 0.73 Å)[33] and Ti^{4+} (VI: 0.605 Å), and both cations are known to exist in a IV square–planar coordination. For the unusual square planar IV coordination of Ti^{4+} in CCTO[34] the ionic radius may be assumed to be similar to that for the Ti^{4+} tetrahedral IV coordination (0.42 Å),[35] because two such ionic radii are reported the same for IV Cu^{2+} as well.[35]

It is clear that the issue of non-stoichiometry in bulk CCTO is not resolved yet and clear experimental evidence for any of the above mentioned defect mechanisms [eqn (A–E)] is missing despite considerable research efforts in recent years. The work presented here is therefore intended to shed light on the defect chemistry and non-stoichiometry of CCTO by conducting a phase diagram study. Evidence is presented for two different defect mechanisms, and their corresponding solid solutions, which cause non-stoichiometry in CCTO. Powder and ceramic samples of different composition within the ternary CaO–CuO–TiO_2 phase diagram are analysed, where the CCTO lattice parameter ***a*** and dielectric properties, such as intrinsic bulk resistivity (ρ_b) and permittivity (ε_b), of the ceramics were determined using X-ray diffraction (XRD) and impedance spectroscopy (IS), respectively. It is demonstrated herein, that only by relating such lattice and intrinsic dielectric parameters to each other can exceptionally small levels of CCTO non-stoichiometry be revealed. Data from the individual phase diagram study, lattice parameter determination from XRD and IS experiments alone show no or only inconclusive trends, and a combined study relating the results of all three techniques to each other is required to understand the defect mechanisms, non-stoichiometry and electrical properties of CCTO ceramics. Although evidence for small scale non-stoichiometry in CCTO is presented, the stoichiometric nomenclature of $CaCu_3Ti_4O_{12}$ (CCTO) will be used throughout this work.

II. Experimental

Powders of various compositions within the ternary CaO–CuO–TiO_2 phase diagram were synthesised from different amounts of dried high purity reagents of $CaCO_3$ (Aldrich, 99.995% purity), CuO (Aldrich, 99.99%) and TiO_2 (Sigma-Aldrich, 99.99%). Starting reagents of lower purity were found to be inappropriate for revealing the small intrinsic defect mechanisms in CCTO. Mixing and grinding of the precursor oxides was performed using an agate pestle and mortar. At least 3 successive mixing/grinding and heat treatment cycles were required to fully react and homogenise each composition. The powder reaction was achieved at 1000 °C in a Lenton muffle furnace on Pt foil in successive cycles of 12 and 8 h, until the phase compositions observed by XRD did not change any further. All powders were synthesised simultaneously to exclude differences in the processing conditions. A small portion of each powder was heated again at 1100 °C for 12 h to enable investigation of the phase diagram for both 1100 and 1000 °C fired materials. The former is the most frequently used densification–sintering temperature for CCTO ceramics, whereas CCTO synthesis is most commonly achieved at ≈ 1000 °C. Rapid cooling was performed for all powders by swiftly removing the Pt foils, on which the powders were placed, from the furnace and exposing them to ambient

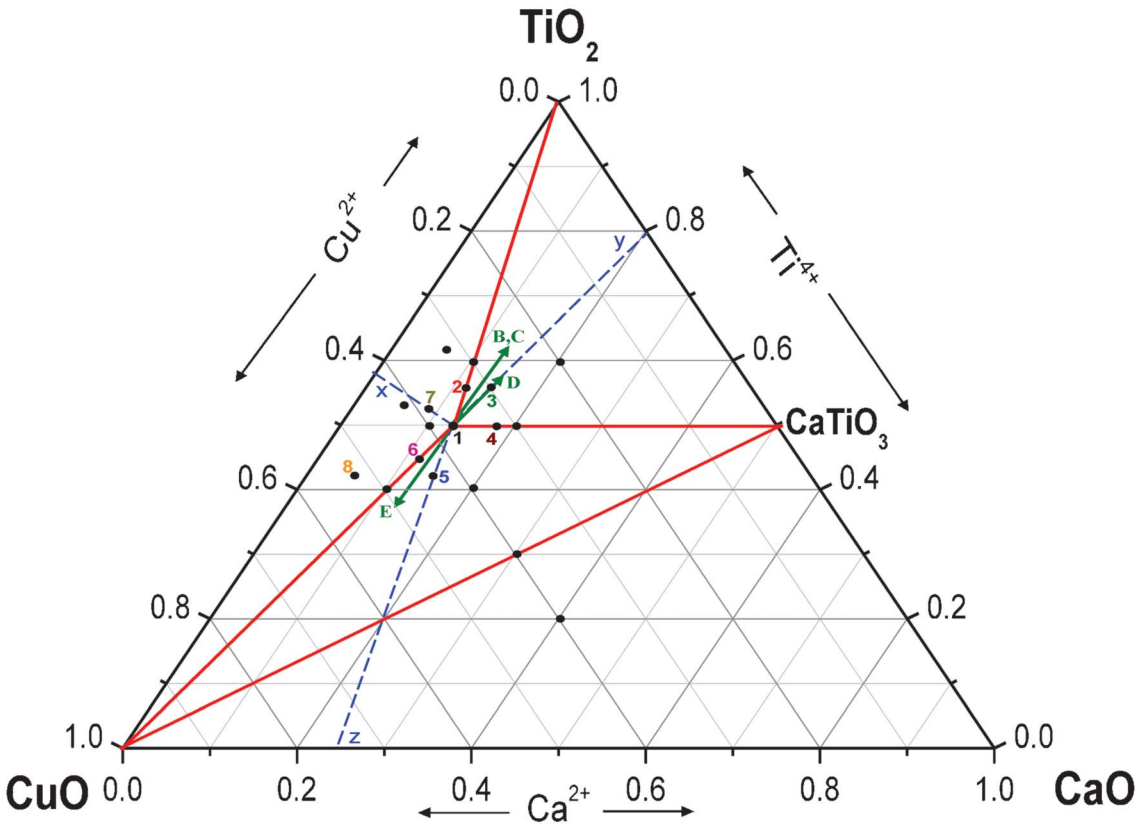

Fig. 1 Ternary CaO–CuO–TiO_2 phase diagram. Filled black symbols represent all of the compositions investigated. Numbered symbols represent the compositions analyzed by the determination of their lattice parameter and IS. On the full red lines two phases are present. Dashed blue lines represent CCTO compositions with potential Ca, Cu or Ti loss: $Ca_{1-x}Cu_3Ti_4O_{12}$, $CaCu_{3-y}Ti_4O_{12}$ and $CaCu_3Ti_{4-z}O_{12}$. Green arrows indicate the direction of the potential solid solutions, see eqn (B–E). Such arrows are much larger than any of the expected small solid solutions and may be regarded as a guide to the eye.

conditions on a brass block. Phase analysis of each composition was performed by XRD using a high-resolution STOE STADI-P diffractometer (STOE & Cie GmbH, Darmstadt) with an image plate detector and Cu-Kα1 radiation in transmission mode, operated at 40 kV and 40 mA. Data were collected using WinXPow® software. Small amounts from all of the 1000 and 1100 °C fired powders were mixed with an internal Si standard, and high angle XRD patterns were collected using the STOE STADI-P diffractometer with a position sensitive detector (PSD). The CCTO lattice parameters were refined from three or more high angle CCTO reflections using a linear least squares fitting routine provided within the WinXPow® software package. For each composition, pellets were pressed from freshly crushed and ground powders using a uni-axial hydraulic press (1 ton) and all were simultaneously sintered at 1100 °C on Pt foil for 12 h. This is the same holding time used for the 1100 °C phase diagram and the lattice parameter study on the powders. This renders comparable the CCTO 1100 °C powder lattice parameter $\boldsymbol{a}$ and the ceramic dielectric parameters such as intrinsic bulk resistivity (ρ_b) and permittivity (ε_b). As shown below, this is a viable approach to reveal the clear dependencies between $\boldsymbol{a}$–ρ_b and $\boldsymbol{a}$–ε_b.

For dielectric characterisation, pellets were covered on both sides with Au electrodes using a dc sputtering technique. Alternating current IS was carried out at 10–500 K between 1 Hz–2 MHz using an Agilent E4980A LCR meter, a Solartron 1296/1255 impedance analyzer, both with 100 mV amplitude ac voltage signal, an Oxford Instruments closed-cycle He refrigerator and a custom built tube furnace equipped with a Eurotherm 2216 temperature controller. The real and imaginary parts of the complex impedance (Z^*) were measured and converted into the complex capacitance (C^*) and electric modulus (M^*) formats using the standard conversion.[36] Scanning electron microscopy (SEM) images were collected with a JEOL JSM 6400 microscope, which was equipped with a facility for quantitative energy dispersive analysis of X-rays (EDAX). Scanning tunnelling microscopy (STM) micrographs of the ceramic surfaces were collected using a Digital Instrument D3100 atomic force microscope (AFM) with a nanoscope V controller operating in air and equipped with a Conductive Atomic Force Microscopy (C-AFM) module.[37,38]

III. Results

A. Phase analysis in the CaO–CuO–TiO_2 ternary phase diagram

The CaO–CuO–TiO_2 ternary phase diagram for the heat treated powders at 1100 °C is presented in Fig. 1, where the filled

black symbols within the main triangle represent the specific Ca–Cu–Ti cation ratios (at%) of all of the samples investigated. All numbered compositions (1–8) were investigated in more detail by determination of the lattice parameter using XRD and by IS on pellets sintered at 1100 °C.

The only single phase composition detected by XRD phase analysis within the main triangle was the CCTO phase, marked as composition 1. $CaTiO_3$ (CTO) was the only significant single phase on the CaO–TiO_2 binary join. On the solid (red) lines within the main triangle two phases are present, which are the two located at both ends of each line: *e.g.*, CCTO and TiO_2 are present on the line connecting CCTO (composition 1) and the TiO_2 corner. The various smaller secondary triangular regions within the main triangle all contain the three phases located in the corners of these triangles: *e.g.*, CCTO, CTO and TiO_2 are present inside the triangle with corners CCTO, CTO and TiO_2.

Compositions 1–8 were chosen so that the volume concentration of potential secondary phases like CuO, TiO_2 and $CaTiO_3$ would always be well below the percolation threshold for secondary phases randomly distributed within the primary CCTO matrix. This would ensure that the dielectric response in the sintered pellets of all of the labelled compositions would always be dominated by the CCTO phase. The theoretical percolation threshold for a secondary phase is known to be $\approx$ 16%,[39] whereas experimental values are commonly reported to be up to $\approx$ 20%.[40]

No direct evidence for two different CCTO compositions is found in the phase diagram, *i.e.*, for the GB and bulk CCTO phases. The phase relationships detected are consistent with the notion that no major defect mechanism and related solid solution are directly obvious and that CCTO and CTO are the only non-trivial single phase compositions in agreement with recently published work.[41] Therefore, the solid solutions potentially causing the non-stoichiometry listed above in eqn (A–E) would be small and are indicated by the green arrows in Fig. 1. For demonstration purposes the length of the (green) arrows is depicted as being much larger than the small extent to which the solid solutions would be expected to be developed.

Unclear results were obtained within the triangle with corners CuO, CTO and CaO, where the phase relationships could not be determined unambiguously. No signs of CaO and Ca_2CuO_3 were detected, in contrast to previous reports on 950 °C heat treated powders.[41] The compositions in this triangle were prone to extensive partial melting of CuO and possibly Ca containing phases other than CaO and Ca_2CuO_3 were formed. In fact, none of the compositions investigated showed any sign of CaO formation. The XRD patterns and SEM micrographs for all of the numbered compositions (Fig. 1) are displayed in the ESI, parts I(a) and (b).†

The phase diagrams for the heat treatments at 1000 and 1100 °C were found to be identical, with one exception: no crystalline CuO phase could be detected at 1100 °C in any composition by powder XRD, whereas at 1000 °C crystalline CuO was detected in all compositions, where it was expected [see ESI, part I(a)†]. It is suggested that CuO may partially melt at 1100 °C, which was confirmed in the CuO-rich pellets, where a Cu-rich phase precipitated out of the pellets during sintering at 1100 °C and remained on the Pt foil after cooling. No CuO phases could be detected in these pellets using XRD phase analysis, although some partially melted CuO may still be present in the GB areas and could remain amorphous or micro-crystalline after cooling and, therefore, cannot be detected by XRD.

The presence of a highly conductive Cu-rich phase was also confirmed on the surface of the pellet of composition 6 using C-AFM as presented in the ESI [part I(c)]†. It should be mentioned that the proposed partial melting and precipitation process of CuO may also occur, to a smaller extent, during synthesis of CCTO at 1000 °C. This may have prevented the full chemical reaction of CuO with the remaining precursors, which could serve as a plausible explanation for the unexpected finding of small amounts of $CaTiO_3$ in certain compositions (Table 1). In the case of such Cu deficiency and concomitant unexpected $CaTiO_3$ residues, some residual TiO_2 would be expected as well for stoichiometric reasons. In composition 1 no TiO_2 was detected, which may favour the mechanism in eqn (B) listed above or imply an unusual Ti-rich $CaTiO_3$ phase. All phases detected for the 1100 °C powders and their expected phase compositions are summarised in Table 1, together with all of the powder CCTO lattice parameters ***a*** at 1100 and 1000 °C. It is evident that ***a*** is generally larger for the samples heat treated at 1100 °C, possibly due to the partial reduction of cations and concomitant increase in the cationic radii, *e.g.*, $Ti^{4+} \rightarrow Ti^{3+}$, or $Cu^{2+} \rightarrow Cu^{+}$. This finding may favour

Table 1 In 6 columns: 1) composition number; 2) nominal cation ratio (atomic fractions); 3) expected phase concentration using the lever rule (wt fractions); 4) detected phase compositions from the 1100 °C samples: brackets are used to indicate small [ ] or very small [[ ]] signs of an unexpected phase detected using EDAX; the CuO phase is written in *italics* for compositions where it was expected from the phase diagram, but missing from the XRD analysis; 5) lattice parameters after firing at 1100 °C and, 6) 1000 °C, where brackets ( ) contain the error in ***a*** for the last digit displayed from the linear least squares fitting routine

Compos. number	Cation ratio (fractions)	Expected phases (wt)	Detected phases (1100 °C)	***a***/Å (1100 °C)	***a***/Å (1000 °C)
1	Ca 0.125, Cu 0.375, Ti 0.5	CCTO (1)	CCTO, [CTO]	7.3925 (1)	7.3916 (4)
2	Ca 0.11, Cu 0.33, Ti 0.56	CCTO (0.88), TiO_2 (0.12)	CCTO, TiO_2, [[CTO]]	7.3928 (1)	7.3917 (3)
3	Ca 0.14, Cu 0.3, Ti 0.56	CCTO (0.84), CTO (0.07), TiO_2 (0.09)	CCTO, CTO, TiO_2	7.3924 (3)	7.3905 (2)
4	Ca 0.175, Cu 0.325, Ti 0.5	CCTO (0.88), CTO (0.12)	CCTO, CTO	7.3931 (2)	7.3925 (3)
5	Ca 0.145, Cu 0.435, Ti 0.42	CCTO (0.74), CuO (0.17), CTO (0.09)	CCTO, CTO, *CuO*	7.3922 (2)	7.3929 (2)
6	Ca 0.1125, Cu 0.4375, Ti 0.45	CCTO (0.9), CuO (0.1)	CCTO, [CTO], *CuO*	7.3929 (4)	7.3911 (2)
7	Ca 0.1025, Cu 0.385, Ti 0.5125	CCTO (0.81), CuO (0.08), TiO_2 (0.11)	CCTO, TiO_2, [CTO], *CuO*	7.3915 (1)	7.3903 (2)
8	Ca 0.06, Cu 0.52, Ti 0.42	CCTO (0.47), CuO (0.35), TiO_2 (0.18)	CCTO, TiO_2, [CTO], *CuO*,	7.3912 (2)	7.3905 (3)

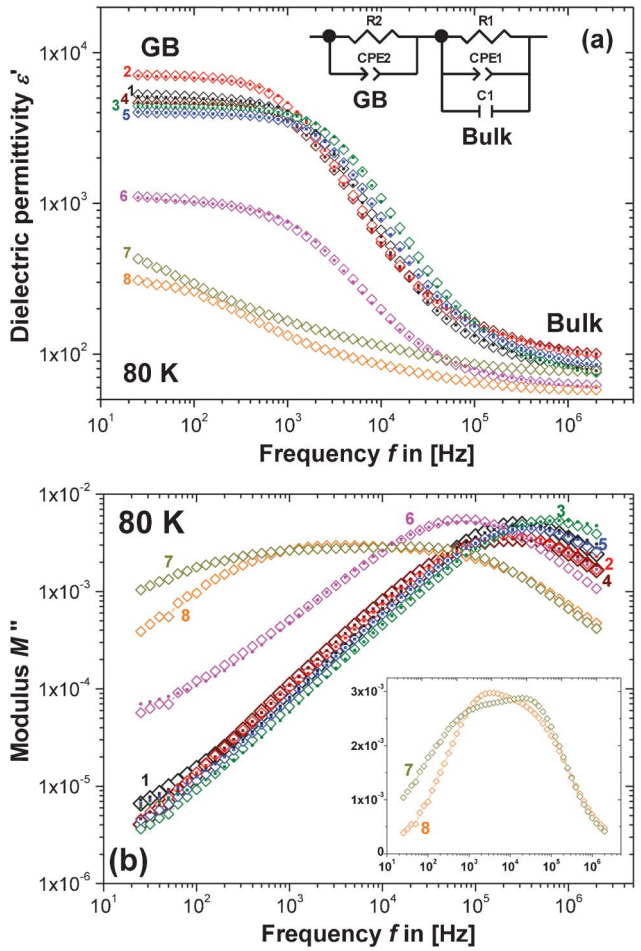

Fig. 2 IS data for the 1100 °C sintered pellets of compositions 1–8 at 80 K, plotted on double-logarithmic axes of (a) the real part concerning the dielectric permittivity (ε') *vs.* frequency (f), and (b) the imaginary part concerning the electric modulus (M'') *vs.* f. Open diamonds (◇) represent experimental data, while the filled dots (•) represent the fit to the equivalent circuit model shown in the inset of part (a). The inset of part (b) shows M'' *vs.* f for compositions 7 and 8 on semi-logarithmic axes.

defect mechanisms involving high temperature cationic reduction, *i.e.,* those in eqn (A) and (B).

For the 1100 °C fired powders it can be seen that the Cu containing compositions, 7 and 8, show smaller lattice parameters than compositions 1–6. This was regarded as an initial indication that the bulk CCTO may indeed exhibit Cu non-stoichiometry. However, the changes in lattice parameter for the different compositions are rather small (the maximum difference in the 1100 °C powders is 0.026%) and no conclusive trend between all of the other compositions is evident from their lattice parameters alone.

B. Impedance spectroscopy (IS)

Fig. 2 shows the IS data obtained from the 1100 °C sintered pellets of composition 1–8 at 80 K using the formalism of the real part of the dielectric permittivity, ε' *vs.* the frequency, f (Fig. 2a), and the imaginary part of the electric modulus, M'' *vs.* f (Fig. 2b). The data have been fitted to the equivalent circuit model shown in Fig. 2a, which is discussed in more detail in section C. Fig. 2a displays two permittivity plateaus at high- and low-frequency as a result of the electronic heterogeneity of the pellets. This is well understood, for the single phase ceramic CCTO in terms of the typical IBLC structure.[13] The low-frequency and high-permittivity plateau is interpreted as a GB effect and the high-frequency and low-permittivity plateau represents the intrinsic bulk.[9] This interpretation requires that the brick-work layer model is valid and each relaxation can be described using a parallel resistor–capacitor element (RC element), and a possible equivalent circuit model would consist of a series of such RC elements.[42,43] Fitting such a model to the data allows discrimination and separate analysis of the grain interior and GB dielectric response.

It is obvious from Fig. 2 that different secondary phases have a distinct influence on the dielectric behaviour and the IS data fall into two categories: Compositions 7 and 8 differ from 1–5, whereas 6 shows an intermediate dielectric response and may fall in between these two groups. According to the phase diagram in Fig. 1, compositions 7 and 8 belong to the same compositional triangle (CuO–CCTO–TiO_2), which would be a plausible explanation for their dielectric distinction. Below in section III(D) it will be shown that this interpretation is incomplete: compositions 5 and 6 also differ from 1–4 when their dielectric response is related to the CCTO lattice parameter ***a***. It appears that it is in fact the presence or absence of the CuO secondary phase that separates the investigated compositions, according to their dielectric response, into two categories: i) 1, 2, 3, 4 (no extra CuO); and ii) 5, 6, 7 and 8 (with extra CuO). From Fig. 2a it can be seen that the low-frequency and high-permittivity plateau, which is associated with the GB permittivity, varies strongly with the composition. Such a variation may express changes in the GB composition and/or variation in the GB thickness. Discrimination between these two explanations is not possible, but a major influence from the grain size can be excluded. It is demonstrated in the ESI [part I(b)]†, that the grain size only slightly varies with changes in the composition.

The variations in the IBLC structure demonstrated in Fig. 2a for the different compositions will be analysed in detail in the following section in order to obtain information on potential defect mechanisms and solid solutions that are present. In several previous studies, the effect of secondary phases on the CCTO giant dielectric permittivity had been analysed in detail, but the giant permittivity is extrinsic in nature. Those analyses therefore gave phenomenological information only and the investigation of the intrinsic bulk dielectric relaxation was carried out in this work to gain fundamental insight into the potential intrinsic changes of the CCTO phase induced by the presence of different secondary phases.

For the analysis of the intrinsic bulk dielectric relaxation it is advantageous to display IS data in terms of the electric modulus formalism as plots of M'' *vs.* f (Fig. 2b). This is because each dielectric relaxation is shown as a relaxation peak in the M'' *vs.* f plots, where the relaxation with the smallest capacitance (bulk) exhibits the largest peak.[42] In contrast, for the conventional impedance $-Z''$ *vs.* f plot the dielectric relaxation peak for the relaxation with the largest resistance in the sample (GB) is the most pronounced.[42] The

approximate peak frequencies for the GB and bulk relaxation peaks are given in eqn (1) for the respective plots of $-Z''$ *vs.* f (GB) and M'' *vs.* f (bulk), using two ideal RC elements connected in series. Eqn (1) implies that an extrinsic GB-type relaxation with large resistance and capacitance would appear at a lower f than the bulk, which is a common feature in the experimental impedance spectra of electroceramics. The different ordinates of the GB and bulk relaxation peaks are shown in eqn (2) for a typical CCTO scenario with distinct differences between the GB and bulk RC elements.

$$f_{\max}(-Z'') \approx \frac{1}{2\pi R_{GB} C_{GB}} = \frac{1}{2\pi \rho_{GB} \varepsilon_0 \varepsilon_{GB}};$$
$$f_{\max}(M'') \approx \frac{1}{2\pi R_b C_b} = \frac{1}{2\pi \rho_b \varepsilon_0 \varepsilon_b} \quad (1)$$

$$-Z''(f_{\max}) \approx \frac{R_{GB}}{2} = \frac{\rho_{GB}}{2g}; M''(f_{\max}) \approx \frac{C_0}{2C_b} = \frac{1}{2\varepsilon_b} \quad (2)$$

C_0 and ε_0 represent the capacitance of the empty measuring cell in a vacuum and the dielectric permittivity of a vacuum, respectively. The geometrical factor g is derived from the pellet surface A divided by the pellet thickness d ($g = A/d$). R_{GB}, C_{GB} and R_b, C_b represent the resistance and capacitance of the GB and bulk areas, respectively, whereas ρ_{GB}, ε_{GB} and ρ_b, ε_b correspond to the respective specific parameters of resistivity and dielectric permittivity. The differences in the peak ordinates in eqn (2) guarantee that for $-Z''$ *vs.* f the relaxation peak representing the largest resistivity (ρ_{GB}) and for M'' *vs.* f the peak representing the smallest permittivity (ε_b) are the most strongly pronounced.

M'' *vs.* f data are plotted on double-logarithmic axes in Fig. 2b. For compositions 1–5 only one high f relaxation peak is displayed, which is indicative of a conventional CCTO bulk dielectric relaxation process. Compositions 7 and 8 appear to display a flat peak response for M'' *vs.* f, but it is in fact a double peak response (see Fig. 2b, inset) and the bulk dielectric response seems to be distinctly different, whereas composition 6 falls in between these two types of responses. Again, as mentioned above, this interpretation is incomplete and the categories are divided into i) 1–4; and ii) 5–8. Notably, the impedance spectra of 7 and 8, as well as all of the other compositions, display two additional relaxation processes, GB and electrode contributions, which are not visible in Fig. 2a and b, but are at higher temperatures [ESI, part II(a) and (b)†]. Therefore, neither of the double peaks in 7 and 8 are likely to represent a GB or electrode relaxation and may well be associated with two different bulk CCTO contributions or one CCTO contribution and a secondary phase. Since the typical high f bulk dielectric relaxation peak displayed in compositions 1–5 is missing from 7 and 8, it may be plausible that the peak with the higher f of the two double-peaks is more likely to represent the main bulk CCTO relaxation of composition 7 and 8. A complete absence of the CCTO bulk relaxation is unrealistic due to the XRD patterns clearly displaying the CCTO phase, which strongly dominates over all of the secondary phases.

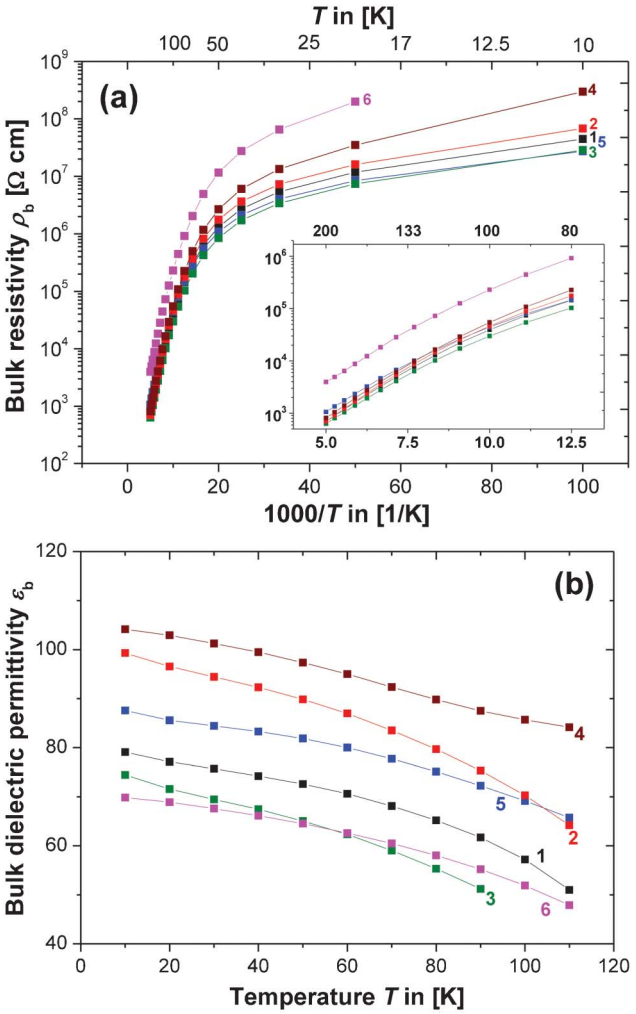

Fig. 3 Plots showing the temperature trends of the equivalent circuit parameters R1 and C1: (a) logarithmic bulk resistivity ρ_b (in Ω cm) *vs.* reciprocal temperature 1000/T (in 1/Kelvin). Inset: Magnification of the high temperature data; axes and colour codes are identical to the main figure. (b) Bulk relative dielectric permittivity ε_b *vs.* T (in Kelvin).

Furthermore, it is important to consider that the double-peaks both occur at a significantly lower f compared to the bulk peaks for compositions 1–5. If it is assumed that each relaxation can be described by an RC element, the height of the relaxation peaks in Fig. 2b would be proportional to the reciprocal dielectric permittivity ε_b (eqn (2)), whereas the peak frequency is proportional to $R_b \times C_b$, or $\varepsilon_b \times \rho_b$ (see eqn (1)). This implies that the two processes in composition 7 and 8, represented by the two M'' *vs.* f double-peaks, both exhibit significantly increased ρ_b when compared to the single CCTO bulk relaxations for composition 1–5. The typical CCTO semiconducting bulk relaxation at high f is missing. Therefore, ρ_b must be strongly increased, because the typical low resistivity bulk CCTO relaxation process would be observable at high f, as in compositions 1–5, even in the presence of secondary phases, but no such observation was made. This was regarded as a further indication that the dielectric heterogeneity of CCTO is a result of the non-

stoichiometry of Cu. The relaxation peak of composition 6 indicates an increased resistivity, as well as being consistent with the presence of secondary phase CuO.

Due to strong relaxation peak broadening and overlap, the double peaks in composition 7 and 8 cannot be modelled using two bulk-type RC elements connected in series.

C. Equivalent circuit fitting

The impedance data from the 1100 °C sintered pellets of compositions 1–5 were fitted to the equivalent circuit model shown in Fig. 2a, which had been successfully applied before.[14,44] Bulk and GB relaxations were represented by RC elements. The intrinsic bulk dielectric relaxation process was fitted to a standard RC element, *i.e.*, an ideal resistor (R1) and capacitor (C1) in parallel[45] and an additional constant-phase element (CPE) in parallel (CPE1). The use of such a CPE has been shown previously to be appropriate to account for non-ideal bulk relaxations in electroceramics.[46] The extrinsic GB relaxation was fitted with a non-ideal RC element (R2–CPE2) where the ideal capacitor was replaced with a CPE (CPE2). Non-ideal R–CPE or R–CPE–C circuits indicate a broadening of the respective dielectric relaxation peak as a reflection of the broadening of the distribution of relaxation times, τ.[47] In an ideal RC element τ is derived from: $\tau = RC = \rho\varepsilon_0\varepsilon$.

The two non-ideal RC elements were connected in series according to the brick-work layer model,[43] and the data and model in Fig. 2a and b show good agreement. An equivalent circuit fit to composition 6 was also successfully carried out. The fitting errors were larger here, which may well be a reflection on the less ideal dielectric behaviour that was demonstrated in the M'' *vs.* f plot (Fig. 2b).

The fitted bulk resistivity (ρ_b) and capacitance (ε_b) are plotted in Fig. 3a and b. The data could not be corrected for pellet porosity because the theoretical density was not accessible due to the mixed phase of the compositions and the potential Cu loss. Due to the high 1100 °C sintering temperature the pellet densities were assumed to be close to the theoretical value. In the case of composition 1, with a nominal single phase of CCTO, the experimental density was calculated to be 100%. In all other compositions CCTO is the major phase and CCTO grains were expected to sinter to a similarly high density. The ρ_b values are displayed as Arrhenius plots of logarithmic ρ_b *vs.* the reciprocal temperature $1000/T$ (Fig. 3a). All of the $\ln(\rho_b)$ *vs.* $1000/T$ curves show two distinct features: (1) a change in the general trend is evident near 80 K and conduction seems to undergo a transition; (2) differences between the various compositions are more distinct below 80 K.

It has been shown that at low temperatures ($T \leqslant 100$ K) the electrical conduction in semiconductors is often dominated by impurities.[48] The change of slope in all of the $\ln(\rho_b)$ *vs.* $1000/T$ curves may be explained by a transition into an impurity conduction regime upon cooling to $T \leqslant 80$ K. Since the pellets all have different compositions it is plausible that conduction varies more strongly at $T \leqslant 80$ K in the impurity conduction regime where additional phases may have a stronger impact. Above 80 K electrical conduction may be dominated by the bulk CCTO phase and, therefore, the curves for compositions 1–5 are similar. The trends in the $\ln(\rho_b)$ *vs.* $1000/T$ curves show

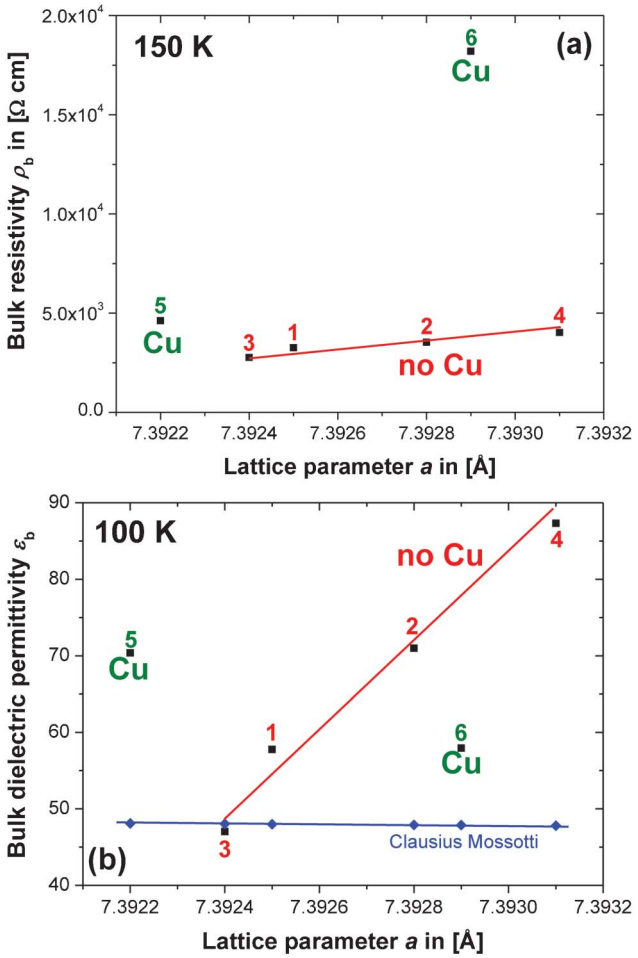

Fig. 4 Plots showing the trends in (a) the bulk resistivity ρ_b from the equivalent circuit fits *vs.* the lattice parameter ***a*** for compositions 1–6 (■), and (b) the bulk dielectric permittivity, ε_b, from the equivalent circuit fits *vs.* ***a*** (■). Estimations for ε_b in CCTO (◆) were obtained using the Clausius–Mossotti equation.

only small quantitative differences for $T > 80$ K, whereas composition 6 deviates. Additional Cu increases the CCTO bulk resistivity as mentioned previously.

The capacitance C1 is shown as the plot of dielectric permittivity ε_b *vs.* T in Fig. 3b. It should be noted that the equivalent circuit component C1 represents the high-frequency, low-permittivity plateau, but it is not equal to the intrinsic bulk permittivity. C1 contains a small contribution from the GB permittivity and can be corrected accordingly. This correction procedure has been carried out successfully on the IS data for Sr-doped CCTO,[10] but it was found here that such a correction would change ε_b only marginally below the experimental error and equivalent circuit fitting errors. The sintering temperature (1100 °C) was higher here compared to the 1000 °C used in ref. 10, which led to a much more pronounced IBLC structure. As a consequence, we find larger differences between the GB and bulk permittivity and the GB permittivity has only a marginal effect on the bulk value. In Fig. 3b the uncorrected ε_b values are shown.

The apparent increase of ε_b (Fig. 3b) with reducing temperature can be explained either by incipient ferroelec-

tricity or a charge–transfer mechanism.[49] Such behaviour in CCTO has been reported previously,[50] and is confirmed here. All of the trends in the ε_b *vs.* T curves are qualitatively similar and only quantitative variations are evident. Such quantitative differences are difficult to interpret from Fig. 3b alone. In the next section it will be demonstrated that such differences are correlated with the CCTO lattice parameter ***a***.

D. Combined analysis of lattice and dielectric parameters

Summarising the results from the above section, indications have been found in the impedance spectra that the potential non-stoichiometry in CCTO may involve Cu. In this section clear trends between the bulk resistivity ρ_b *vs.* lattice parameter ***a*** and bulk dielectric permittivity ε_b *vs.* ***a*** are presented and at least two different defect mechanisms and associated solid solutions in CCTO are revealed.

i) Cu-deficient compositions. Fig. 4a shows a plot of bulk resistivity ρ_b for compositions 1–6 (obtained from equivalent circuit fits) *vs.* the lattice parameter ***a*** (determined from high resolution powder XRD). For compositions 1–4, ρ_b at 150 K shows a modest and approximately linear increase with ***a***. It is unclear at this point whether this increase of ρ_b with ***a*** represents a solid solution, because the increase is small and may simply be a consequence of the increasing atomic distance of the cations. With increasing ***a*** the orbital overlap may reduce leading to higher ρ_b.

Compositions 5 and 6 do not follow the same trend and their ρ_b values seem to be elevated. The curves of ρ_b *vs.* ***a*** for compositions 1–6 at alternative temperatures of 20, 50 and 100 K all show equivalent features. This confirms that the presence of extra Cu in 5 and 6 leads to a higher bulk ρ_b compared to compositions 1–4. The highly resistive GB regions may contain a higher Cu content than the semiconducting Cu-deficient bulk.

The trend for the dielectric permittivity, ε_b, obtained from the equivalent circuit fits *vs.* ***a*** is presented in Fig. 4b, where the dielectric data have been collected at 100 K. The main feature of this data is the increase in dielectric permittivity ε_b with ***a*** for compositions 1–4, which cannot be explained by a simple lattice expansion. The Clausius–Mossotti equation predicts an approximately constant $\varepsilon_b \approx 48$, taking into consideration the small changes in ***a*** observed and the atom polarizabilities obtained from ref. 19. The secondary phases in compositions 1–4, $CaTiO_3$ and/or TiO_2, both have a lower permittivity than CCTO and, therefore, cannot cause such an anomalous increase in ε_b directly, but may well influence the defect mechanism in the CCTO bulk phase responsible for the ε_b increase to $\approx$ 100. If it were the case that the secondary phase of CuO simply extends the existing defect mechanism for compositions 1–4 to higher Cu contents, compositions 5 and 6 would be expected to fall onto the same line as 1–4, which is clearly not the case, therefore, one or more additional defect mechanisms may well exist. The mechanism detected for compositions 1–4 may not involve large differences in Cu content because, in this case, a larger variation of ρ_b with ***a*** than that detected in Fig. 4a would be expected. Additionally, significant changes in the oxygen content are unlikely, because the concomitant changes in cationic valence would also be expected to lead to larger variations in ρ_b.

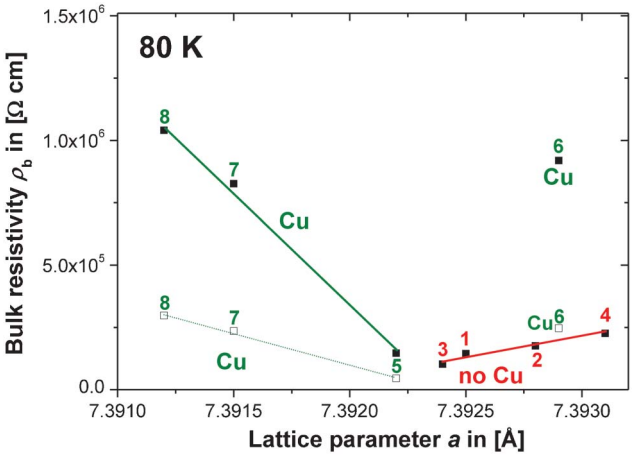

Fig. 5 Trends of ρ_b *vs.* ***a*** for all compositions (1–8) derived from the equivalent circuit fits (■) and from estimates obtained from the M'' *vs.* f relaxation peak analysis (□). For compositions 7 and 8 the ρ_b values (■) were multiplied by a constant correction factor (3.5), which was approximated from the difference in ρ_b for compositions 5 and 6 obtained from; (i) the M'' method and (ii) the equivalent circuit fits.

ii) Cu-rich compositions. To elucidate the role of the secondary CuO phase on the CCTO bulk resistance, ρ_b values for all compositions containing extra CuO (5–8) were estimated from the relaxation peak height and peak position in the M'' *vs.* f plots (Fig. 2b) according to eqn (1) and (2).

For the double-peaks in compositions 7 and 8 estimates were taken from the peak at a higher f in the M'' *vs.* f plots, which was argued above to be more likely to represent the main CCTO bulk relaxation. The estimated ρ_b values obtained from the M'' *vs.* f plots for compositions 5 and 6 were compared to the respective ρ_b values from the equivalent circuit fits [see section III(C)]. It was found that at 80 K the estimated ρ_b values were smaller by a factor of 3.23 (composition 5) and 3.72 (composition 6) than the values from the equivalent circuit fits. This can be explained by the non-ideality of the relaxation processes leading to a broadening of the relaxation peaks in M'' *vs.* f. This, in turn, leads to a reduction in peak height and an overestimate of ε_b according to eqn (2). The error made in the estimation of ρ_b from the M'' *vs.* f plots was approximated to be a uniform factor of $\approx$ 3.5. Thus, the estimated values (□ in Fig. 5) for compositions 7 and 8 were multiplied by a factor of 3.5 in order to account for the estimation error. Both, the uncorrected (□) and corrected (■)ρ_b values for compositions 7 and 8 at 80 K are plotted *vs.* ***a*** in Fig. 5 and approximately fall onto one line with composition 5 displaying a significant increase in ρ with decreasing ***a***. Composition 6 is an exception to this trend, which is probably an experimental error or artefact. Still, the significant ρ_b increase with decreasing ***a*** detected in the Cu-rich samples 5, 7 and 8 strongly suggests the existence of a second defect mechanism and an associated solid solution. This mechanism may well relate the large differences between the GB and bulk resistivity to the Cu concentration: the GB regions would be Cu-rich and bulk regions Cu-deficient. Or, in other terms, the GB regions would exhibit compositions with a higher Cu-

content, possibly quite close to the stoichiometric and nominally insulating CCTO phase, in contrast to the Cu-deficient bulk. The defect mechanisms mentioned above in eqn (B–D) involve Cu deficiency, but from the data presented here a clear discrimination is difficult. In agreement with the indications mentioned above, the mechanisms in eqn (B) and (C) may be favourable though, because the increase in $\boldsymbol{a}$ with decreasing ρ_b for the Cu-rich compositions (5–8), displayed in Fig. 5, may be inconsistent with the mechanism in eqn (D).

IV. Summary and discussion

Combined analysis of the XRD lattice parameter $\boldsymbol{a}$ and IS data revealed approximately linear relationships between the CCTO bulk resistivity ρ_b *vs.* $\boldsymbol{a}$ and the intrinsic bulk dielectric permittivity ε_b *vs.* $\boldsymbol{a}$. For Cu-deficient compositions 1–4, an anomalous increase of the CCTO bulk dielectric permittivity ε_b with $\boldsymbol{a}$ was found, above that predicted using the Clausius–Mossotti equation, as a result of a distinct defect mechanism.

Compositions 5–8 containing a CuO secondary phase did not follow the same trends. The presence of excess CuO led to an increased ρ_b and indications of a second defect mechanism were found, which may explain the large difference between the GB and bulk resistivity in terms of the difference in Cu content. This would most likely be associated with the defect mechanisms in eqn (B) and (C), mentioned in section I. For compositions 1–4 the source of their semiconductivity in the respective CCTO bulk phase may also be due to Cu deficiency, but it may be independent of the TiO_2 and/or $CaTiO_3$ secondary phases since no large differences in ρ_b were detected.

The rather small increase of ρ_b with $\boldsymbol{a}$ in compositions 1–4 (Fig. 5a) leads to some further important conclusions: the underlying defect mechanism causing high ε_b may not involve any large changes in the cationic valence of Cu and/or Ti, in which case larger differences in ρ_b would be likely. This would exclude major contributions from all of the mechanisms mentioned above in eqn (A–D), except for the mechanism shown in eqn (E), which concerns a Cu excess compensated for by the formation of oxygen vacancies. Since compositions 1–4 are all Cu-deficient, the mechanism in eqn (E) is unlikely. Instead, the formation of anti-site defects like Ca–Cu, Cu–Ti or Ca–Ti inter-site cation exchanges may be a more plausible explanation. Evidence for Ca–Cu anti-site disorder has indeed been reported in the literature,[32,51] although it should be noted that, in this work, the Ca–Cu anti-site defects are proposed to serve as an explanation for the increased bulk permittivity ε_b and not for the extrinsic giant permittivity ε_{GB}.

The trends seen in ρ_b *vs.* $\boldsymbol{a}$ and ε_b *vs.* $\boldsymbol{a}$ are relatively uniform for all of the compositions investigated, which may be a result of the identical powder synthesis and pellet sintering conditions employed. The two distinct defect mechanisms detected were only obvious from combined analysis of $\boldsymbol{a}$ and the IS data, and cannot be clearly identified otherwise. From the difficulty of detection it is obvious that the extent to which the defect mechanisms in CCTO ceramics are developed may be small and difficult to control.

V. Conclusions

Compositions in the CaO–CuO–TiO_2 phase triangle without a CuO secondary phase exhibit an anomalous increase of the CCTO bulk dielectric permittivity ε_b with $\boldsymbol{a}$ above the values predicted from the Clausius–Mossotti equation. This was associated with a defect mechanism based on Ca–Cu anti-site defects, which causes a high intrinsic bulk dielectric permittivity. Compositions containing a CuO secondary phase exhibit increased resistivity. A second mechanism is proposed to be responsible for the large difference between the GB and bulk resistivity in CCTO: GB areas may be Cu-rich, whereas bulk areas may be Cu-deficient. Such Cu gradients may well develop during the ceramic sintering processes.[21]

Acknowledgements

The authors acknowledge funding from the European Union under the NUOTO project and grant agreement no. 226716 (FP7/2007-2013). DCS thanks the EPSRC (UK) for funding (EP/G005001/11). RS acknowledges a Ramón y Cajal fellowship from the MINECO (Spain).

References

1 M. A. Subramanian and A. W. Sleight, *Solid State Sci.*, 2002, **4**, 347.
2 A. P. Ramirez, M. A. Subramanian, M. Gardel, G. Blumberg, D. Li, T. Vogt and S. M. Shapiro, *Solid State Commun.*, 2000, **115**, 217.
3 A. M. Glazer, *Acta Crystallogr., Sect. B: Struct. Crystallogr. Cryst. Chem.*, 1972, **28**, 3384.
4 S. H. Byeon, S. S. Lee, J. B. Parise and P. M. Woodward, *Chem. Mater.*, 2006, **18**, 3873.
5 L. Wu, Y. Zhu, S. Park, S. Shapiro, G. Shirane and J. Tafto, *Phys. Rev. B: Condens. Matter Mater. Phys.*, 2005, **71**, 014118.
6 M. A. Subramanian, D. Li, N. Duan, B. A. Reisner and A. W. Sleight, *J. Solid State Chem.*, 2000, **151**, 323.
7 C. C. Homes, T. Vogt, S. M. Shapiro, S. Wakimoto and A. P. Ramirez, *Science*, 2001, **293**, 673.
8 S.-Y. Chung, I.-D. Kim and S.-J. L. Kang, *Nat. Mater.*, 2004, **3**, 774.
9 T. B. Adams, D. C. Sinclair and A. R. West, *Adv. Mater.*, 2002, **14**, 1321.
10 R. Schmidt and D. C. Sinclair, *Chem. Mater.*, 2010, **22**, 6.
11 V. Brizé, G. Gruener, J. Wolfman, K. Fatyeyeva, M. Tabellout, M. Gervais and F. Gervais, *Mater. Sci. Eng., B*, 2006, **129**, 135.
12 A. R. West, T. B. Adams, F. D. Morrison and D. C. Sinclair, *J. Eur. Ceram. Soc.*, 2004, **24**, 1439.
13 D. C. Sinclair, T. B. Adams, F. D. Morrison and A. R. West, *Appl. Phys. Lett.*, 2002, **80**, 2153.
14 P. Lunkenheimer, R. Fichtl, S. G. Ebbinghaus and A. Loidl, *Phys. Rev. B: Condens. Matter Mater. Phys.*, 2004, **70**, 172102.
15 T. B. Adams, D. C. Sinclair and A. R. West, *Phys. Rev. B: Condens. Matter Mater. Phys.*, 2006, **73**, 094124.
16 M. C. Ferrarelli, D. C. Sinclair, A. R. West, H. A. Dabkowska, A. Dabkowski and G. M. Luke, *J. Mater. Chem.*, 2009, **19**, 5916.

17 G. Deng, T. Yamada and P. Muralt, *Appl. Phys. Lett.*, 2007, **91**, 202903.
18 M. Li, Z. Shen, M. Nygren, A. Feteira, D. C. Sinclair and A. R. West, *J. Appl. Phys.*, 2009, **106**, 104106.
19 R. D. Shannon, *J. Appl. Phys.*, 1993, **73**, 348.
20 D. Capsoni, M. Bini, V. Massarotti, G. Chiodelli, M. C. Mozzatic and C. B. Azzoni, *J. Solid State Chem.*, 2004, **177**, 4494.
21 R. Schmidt, M. C. Stennett, N. C. Hyatt, J. Pokorny, J. Prado-Gonjal, M. Li and D. C. Sinclair, *J. Eur. Ceram. Soc.*, 2012, **32**, 3313.
22 I. R. Costa, M. Li, J. R. Frade and D. C. Sinclair, *RSC Adv.*, 2013, **3**, 7030.
23 M. Li, A. Feteira, D. C. Sinclair and A. R. West, *Appl. Phys. Lett.*, 2006, **88**, 232903.
24 J. Li, A. W. Sleight and M. A. Subramanian, *Solid State Commun.*, 2005, **135**, 260.
25 T.-T. Fang, L.-T. Mei and H.-F. Ho, *Acta Mater.*, 2006, **54**, 2867.
26 R. A. De Souza, M. S. Saiful and E. Ivers-Tiffee, *J. Mater. Chem.*, 1999, **9**, 1621.
27 A. R. West, *Basic solid state chemistry*, Wiley: New York, 1988.
28 P. Fiorenza, R. Lo Nigro, A. Sciuto, P. Delugas, V. Raineri, R. Toro, M. Catalano and G. Malandrino, *J. Appl. Phys.*, 2009, **105**, 061634.
29 G. Deng, N. Xanthopoulos and P. Muralt, *Appl. Phys. Lett.*, 2008, **92**, 172909.
30 L. Zhang and Z.-J. Tang, *Phys. Rev. B: Condens. Matter Mater. Phys.*, 2004, **70**, 174306.
31 T.-T. Fang and L.-T. Mei, *J. Am. Ceram. Soc.*, 2007, **90**, 638.
32 Y. Zhu, J. C. Zheng, L. Wu, A. I. Frenkel, J. Hanson, P. Northrup and W. Ku, *Phys. Rev. Lett.*, 2007, **99**, 037602.
33 R. D. Shannon and C. T. Prewitt, *Acta Crystallogr., Sect. B: Struct. Crystallogr. Cryst. Chem.*, 1969, **25**, 925.
34 M. Avdeev and V. B. Nalbandyan, *Inorg. Chem.*, 2006, **45**, 2217.
35 R. D. Shannon, *Acta Crystallogr., Sect. A: Cryst. Phys., Diffr., Theor. Gen. Crystallogr.*, 1976, **32**, 751.
36 *Impedance Spectroscopy*, ed. J. R. Macdonald, John Wiley & Sons, New York, 1987.
37 P. Fiorenza, R. L. Nigro, C. Bongiorno, V. Raineri, M. C. Ferarrelli, D. C. Sinclair and A. R. West, *Appl. Phys. Lett.*, 2008, **92**, 182907.
38 P. Fiorenza, V. Raineri, M. C. Ferrarelli, D. C. Sinclair and R. Lo Nigro, *Nanoscale*, 2011, **3**, 1171.
39 H. Scher and R. Zallen, *J. Chem. Phys.*, 1970, **53**, 3759.
40 B. Vertruyen, R. Cloots, M. Ausloos, J.-J. Fagnard and P. Vanderbemden, *Phys. Rev. B: Condens. Matter Mater. Phys.*, 2007, **75**, 165112.
41 M. Veith, S. Ren, M. Wittmar and H. Bolz, *J. Solid State Chem.*, 2009, **182**, 2930.
42 J. T. S. Irvine, D. C. Sinclair and A. R. West, *Adv. Mater.*, 1990, **2**, 132.
43 R. Schmidt, Impedance Spectroscopy of Electroceramics, in *Ceramic Materials Research Trends*, ed. P. B. Lin, Novascience Publishers, Hauppauge, 2007, p. 321.
44 R. Schmidt, J. Ventura, E. Langenberg, N. M. Nemes, C. Munuera, M. Varela, M. Garcia-Hernandez, C. Leon and J. Santamaria, *Phys. Rev. B: Condens. Matter Mater. Phys.*, 2012, **86**, 035113.
45 J. T. S. Irvine, D. C. Sinclair and A. R. West, *Adv. Mater.*, 1990, **2**, 132.
46 E. J. Abram, D. C. Sinclair and A. R. West, *J. Electroceram.*, 2003, **10**, 165.
47 R. Schmidt, W. Eerenstein, T. Winiecki, F. D. Morrison and P. A. Midgley, *Phys. Rev. B: Condens. Matter Mater. Phys.*, 2007, **75**, 245111.
48 N. F. Mott and W. D. Twose, *Adv. Phys.*, 1961, **10**, 107.
49 C. Kant, T. Rudolf, F. Mayr, S. Krohns, P. Lunkenheimer, S. G. Ebbinghaus and A. Loidl, *Phys. Rev. B: Condens. Matter Mater. Phys.*, 2008, **77**, 045131.
50 Y. Liu, R. L. Withers and X. Y. Wei, *Phys. Rev. B: Condens. Matter Mater. Phys.*, 2005, **72**, 134104.
51 P. Delugas, P. Alippi, V. Fiorentini and V. Raineri, *Phys. Rev. B: Condens. Matter Mater. Phys.*, 2010, **81**, 081104.